Nano Today 61 (2025) 102624

Contents lists available at ScienceDirect

Nano Today

journal homepage: www.elsevier.com/locate/nanotoday

Smart multifunctional $Cu_2O@RuO_2$ nanozyme for angiogenesis and osteogenesis in periodontitis

Yuyang Li [a,b,1], Faheem Muhammad [c,d,1], Xiwen Chen [c,1], Deao Gu [e], Wen Li [a], Jiayi Tang [c], Mingyue Cheng [a], Jiang Du [c], Shuwei Qiao [f], Yu Deng [c], Qing Yu [b], Hui Wei [c,g,*], Leiying Miao [a,**]

[a] Department of Cariology and Endodontics, Nanjing Stomatological Hospital, Affiliated Hospital of Medical School, Research Institute of Stomatology, Nanjing University, Nanjing, Jiangsu 210008, China
[b] Department of Prosthodontics, Nanjing Stomatological Hospital, Affiliated Hospital of Medical School, Research Institute of Stomatology, Nanjing University, Nanjing, Jiangsu 210008, China
[c] Department of Biomedical Engineering, College of Engineering and Applied Sciences, Nanjing National Laboratory of Microstructures, Jiangsu Key Laboratory of Artificial Functional Materials, Nanjing University, Nanjing, Jiangsu 210023, China
[d] Guangdong Key Laboratory of Biomedical Measurements and Ultrasound Imaging, School of Biomedical Engineering, Shenzhen University Medical School, Shenzhen University, Shenzhen 518060, China
[e] Department of Orthodontics, Nanjing Stomatological Hospital, Affiliated Hospital of Medical School, Research Institute of Stomatology, Nanjing University, Nanjing, Jiangsu 210008, China
[f] Department of Prosthetic Dentistry, Hospital of Stomatology, Jilin University, Changchun, Jilin 130021, China
[g] State Key Laboratory of Analytical Chemistry for Life Science, School of Chemistry and Chemical Engineering, Chemistry and Biomedicine Innovation Center (ChemBIC), Nanjing University, Nanjing, Jiangsu 210023, China

ARTICLE INFO

Keywords:
Angiogenesis
Anti-inflammation
Copper
Antioxidant nanozyme
Osteogenesis
Periodontitis
Ruthenium oxide

ABSTRACT

Nanozymes have emerged as promising nanomaterials for the treatment of inflammation-related diseases by eliminating excessive reactive oxide species (ROS) and immunoregulation. However, persistent inflammation invariably causes severe alveolar destruction in periodontitis; and the alleviation of inflammation alone by neglecting the impairment of vascular functions could not effectively realize periodontal regeneration. Herein, a multifunctional copper-ruthenium oxide-based yolk-shell nanozyme ($Cu_2O@RuO_2$, CRNC) is designed to promote effective periodontal regeneration. The ruthenium oxide (RuO_2) shell serves to alleviate inflammation by eliminating ROS and triggering macrophage polarization, whereas the cuprous oxide (Cu_2O) core acts as a responsive Cu^{2+} nano-reservoir for promoting angiogenesis and osteogenesis. Results demonstrated that CRNC could activate transforming growth factor β/phosphatidylinositol 3-kinase (TGF-β/PI3K) and hypoxia-inducible factors (HIF-1α) signals, aiding angiogenesis in the human umbilical vein endothelial cells and osteogenesis in periodontal ligament stem cells, respectively. The multifunctional CRNC nanozyme successfully decreased periodontal inflammation and ameliorated alveolar regeneration in a periodontitis model. This study provides promising insights into periodontitis treatment by targeting both angiogenesis and osteogenesis.

Introduction

Periodontitis (PD) has attracted increasing attention for its chronic inflammatory stimulation, not only causing tooth loss but also jeopardizing systemic diseases, ranking as the sixth most common disease worldwide [1]. Conventional treatments usually depend on mechanical debridement or antibiotic drugs to alleviate inflammation, however, the complexity of periodontal anatomy and the challenge of antimicrobial resistance, severely restrict the therapeutic efficiency [2,3]. Also, the exposure to the oral environment can uncontrollably trigger host

* Corresponding author at: Department of Biomedical Engineering, College of Engineering and Applied Sciences, Nanjing National Laboratory of Microstructures, Jiangsu Key Laboratory of Artificial Functional Materials, Nanjing University, Nanjing, Jiangsu 210023, China.
** Corresponding author.
E-mail addresses: weihui@nju.edu.cn (H. Wei), miaoleiying80@163.com (L. Miao).
[1] These authors contributed equally to this work.

https://doi.org/10.1016/j.nantod.2024.102624
Received 23 October 2024; Received in revised form 4 December 2024; Accepted 26 December 2024
Available online 31 December 2024

immune activation, which in turn ultimately inflicts damage on supporting tissues [4]. Exploration of periodontal treatments with higher efficiency and less invasion to modulate inflammatory response for periodontal reconstruction is highly desirable.

It is well-known that excessive amounts of reactive oxygen species (ROS) (such as H_2O_2, and superoxide anion radicals) production in the PD microenvironment could interrupt antioxidant balance [5]. At the physiological level, the antioxidant system protects against oxidative stress by resolving free radicals, however, during PD progression, the persistent inflammation surpasses the cellular immune defense, drives oxidative stress, and resultantly leads to irreversible alveolar destruction [6]. ROS scavenging to regulate the local microenvironment and rescuing alveolar bone is of great importance for PD treatment. In the past decade, antioxidant nanozymes, with superoxide dismutase (SOD), catalase (CAT), or glutathione peroxidase mimicking activities, have been widely explored for the treatment of oxidative stress-related diseases because of their tunable composition, multifunctionality, high stability, and low cost [7–9]. Multiple studies have shown that the nanozymes-mediated elimination of ROS could efficiently mitigate the inflammatory response and modify the microenvironment [10–12]. Among various nanozymes, notably the exceptionally high catalytic activity, low toxicity, and rich electrochemical and photophysical properties render ruthenium (Ru) containing materials as excellent candidates for the treatment of inflammatory diseases [13]. However, most nanozymes have a single function, limiting the therapeutic requirements for periodontitis which demands the promotion of both angiogenesis and osteogenesis. In earlier studies, targeting only inflammation with ROS-scavenging nanozymes showed some satisfactory results in the short term, but in the long term, complete regeneration was not achieved [14]. Therefore, it is urgent to introduce other functionalities into ROS-scavenging nanozymes for desired alveolar regeneration.

In addition to counter oxidative stress, persistent inflammation also inevitably leads to the impairment of vascular functions. The crosstalk between vascular and osseous tissues is vital for the adequate regeneration of tissues through cellular and molecular regulations [15], as vascular signals accelerate bone remodeling by transporting nutrients and growth factors to mineralized sites [16]. During the development of PD, adverse responses are produced in vascular endothelial cells for the adhesion of immune cells, lipid accumulation, augmented endothelial permeability, and reduction in elasticity, which further aggravate periodontal dysfunction and inhibit tissue healing after the destruction of microcirculation. Therefore, it is also necessary to maintain vascular homeostasis for successful PD treatment [17,18]. Hitherto, most current strategies focus on the improvement of bone quantity, ignoring the restoration of vascular functions.

Copper is a crucial bio-relevant transition metal playing important roles in both cellular and subcellular processes, such as metabolism, lung elasticity, cardiovascular and neuroendocrine functions, and iron metabolism. Recent studies demonstrated that copper also mediates in the improvement of inflammation-related diseases [19]; bone mineralization, and stem cell differentiation [20]. Besides the aforementioned diverse functions, the angiogenic role of copper has also recently been reported via stimulating endothelial cell proliferation, promoting the secretion of vascular endothelial growth factor (VEGF), and ensuring cell migration mediated by cysteine oxidation [21]. It is reported that copper accelerates vascular growth through the accumulation and activation of HIF-α after down-regulation of prolyl hydroxylase [22]. Given the critical role of countering oxidative stress and regeneration of vasculature in PD tissue, herein, we hypothesize that integrating both ROS scavenging and angiogenic features in a single nanoformulation will potentially provide an effective treatment for PD.

To fulfill the above demands, we designed a multifunctional $Cu_2O@RuO_2$ nanozyme (denoted as CRNC) to achieve osteogenesis and angiogenesis for effective periodontal regeneration. In CRNC nanozyme, RuO_2 was chosen to act as an antioxidant nanozyme because of its high stability, and high catalytic performance in scavenging ROS, regulating macrophage polarization, and protecting tissue against overexpressed inflammation [13,23]. RuO_2 was embedded with the pH- and ROS-responsive Cu_2O core, which served as a responsive Cu^{2+}-releasing nanoreservoir. The porous RuO_2 shell also served as a physical barrier to protect the relatively unstable inner Cu_2O core [24,25]. The CRNC nanostructure activated transforming growth factor β/phosphatidylinositol 3-kinase (TGF-β/PI3K) and hypoxia-inducible factors (HIF-1α) signals to promote angiogenesis and osteogenesis. The *in vitro* and *in vivo* studies showed that CRNC significantly reduced the periodontal inflammation and ameliorated alveolar regeneration in the PD model (Fig. 1).

Results and discussion

Preparation and characterization of CRNC nanozyme

The multifunctional CRNC nanozyme was designed using Cu_2O nanocubes as a reactive template [26]. The core-shell nanostructure was prepared by reacting as-synthesized Cu_2O with a concentrated aqueous solution of $RuCl_3$. Subsequently, the yolk-shell nanostructure (CRNC) and hollow RuO_2 nanocubes (RNC) were obtained following different etching treatments (Figure S1). X-ray powder diffraction (XRD) shows the cubic crystal phase of parent Cu_2O with a characteristic pattern (JCPDS No. 05–0667) (Figure S2). The intensities of Cu_2O peaks were dampened and diminished in core-shell and yolk-shell nanostructures, respectively. Scanning electron microscopy (SEM), transmission electron microscopy (TEM), and high-angle annular dark-field scanning transmission electron microscopy (HAADF-STEM) analyses were performed to verify the size, morphology, and elemental compositions of different nanostructures. Fig. 2a-c indicates a nearly monodispersed parent Cu_2O with a cubic morphology, with a particle size of around 150 nm. Inspection of the low-resolution and HRTEM images explicitly proves the polycrystalline nature of Cu_2O. Fig. 2d shows the compositional maps of Cu and O. Notably, the morphology and the size of the Cu_2O template remained almost intact after the formation of $Cu_2O@RuO_2$ core-shell nanocubes. Fig. 2e-g indicates the core-shell nanostructure comprising a Cu_2O core and a porous RuO_2 shell. Besides the presence of crystalline Cu_2O, a disordered crystal structure was also noticed while examining the porous RuO_2 shell (~2 nm), which is in agreement with the XRD results confirming its amorphous nature. The energy-dispersive X-ray (EDX) elemental mapping shows the composition and structure of the core-shell forming components (Fig. 2h). As shown in Fig. 2i-k, the structure of CRNC was also maintained in the next step while producing yolk-shelled nanocubes following the acid-etching process. A relatively reduced amount of copper was detected in the yolk-shell nanostructure, as verified by the EDX mapping analysis (Fig. 2l). The morphology and structure of RNC are shown in Figure S3, indicating hollow-structured nanocubes made of ultrasmall self-assembled porous shell, similar to $Cu_2O@RuO_2$ and CRNC.

The survey X-ray photoelectron spectroscopy (XPS) spectra of parent Cu_2O, $Cu_2O@RuO_2$, and CRNC nanocubes showed their respective compositions (Figure S4). As shown in Fig. 2m, the deconvoluted spectrum of Cu 2*p* of the yolk-shell shows dominant peaks related to Cu^{+} species along with only low amounts of Cu^{2+} species (as shown by the shake-up structure). The XPS signals of Ru 3*p* were deconvoluted into four peaks: two peaks at 463.3 eV and 485.5 eV were attributed to Ru^{4+} and the other two at 465.2 and 487.3 eV were linked to Ru^{3+}. The O 1*s* spectrum of CRNC confirmed the presence of lattice oxygen, hydroxyl groups, and confined water content of RuO_2 (Fig. 2n and o). The deconvoluted spectra of parent Cu_2O and core-shell $Cu_2O@RuO_2$ are shown in Figure S5. Also, zeta potential measurement (Figure S6) and fourier transform infrared spectroscopy (FTIR, Figure S7) were used to further analyze the different nanostructures. The pH- and ROS-responsive dissolution of Cu_2O and the corresponding Cu^{2+} release was determined by exposing the CRNC to 5 mM H_2O_2 and different

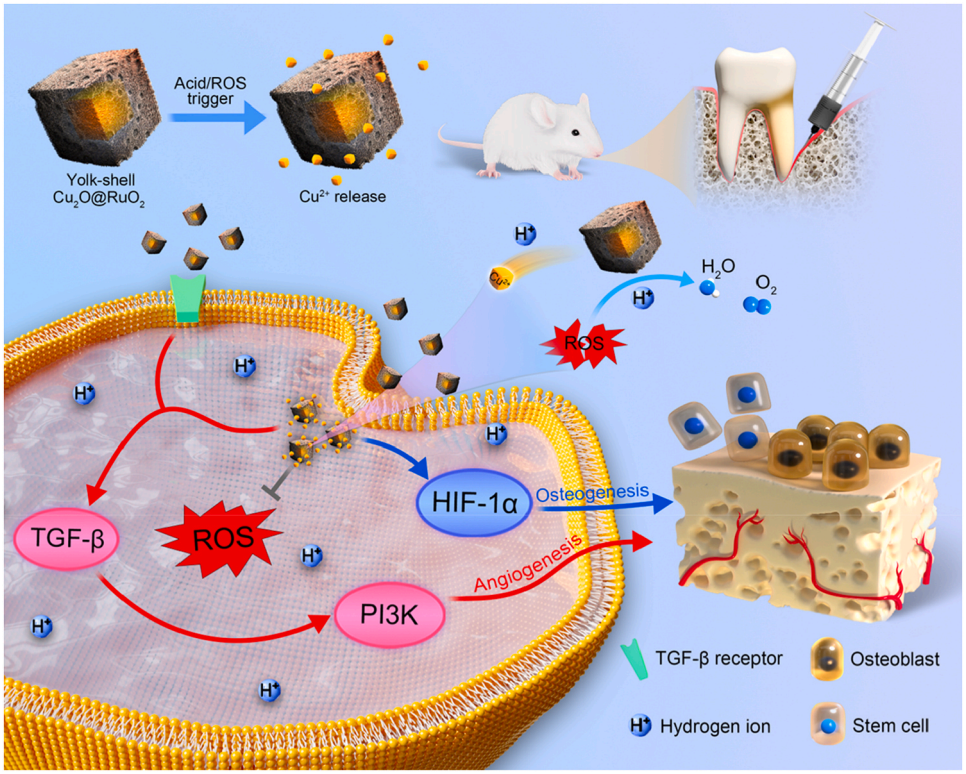

Fig. 1. Schematic illustration of a multifunctional CRNC nanozyme showing its anti-inflammation, angiogenesis, and osteogenesis activities in PD therapy. Upon exposure to acidic and ROS signals, the release of Cu^{2+} from CRNC not only strengthens anti-inflammation but also promotes angiogenesis and osteogenesis by activation of TGF-β/PI3K and HIF-1α signals, respectively, thereby accelerating periodontal regeneration.

acidic media. Figure S8 shows an acid-responsive dissolution of the Cu_2O core, with a decrease in the pH of the solution, a corresponding disintegration of Cu_2O was observed. Besides acid responsiveness, H_2O_2 also accelerated the dissolution of Cu_2O in acidic media. The nitrogen adsorption-desorption isotherms of different nanostructures exhibited type IV features with some hysteresis loops, showing mesoporous structures. Due to the hollow and porous structures, the Brunauer–Emmett–Teller (BET) surface area (S_{BET}) of CRNC was found to be as high as 208 m^2/ g (Figure S9). These porous nanostructures were likely generated from the void space present between self-assembled Cu_2O and ultrasmall RuO_2.

The biocompatibility of RNC and CRNC was first tested in RAW264.7 cells, human umbilical vein endothelial cells (HUVECs), and periodontal ligament stem cells (PDLSCs) (Figure S10). The results showed minimal cellular toxicity of CRNC, as we optimized the copper concentration in that nanostructure to avoid toxicity. Additionally, the biocompatibility of RNC was also found to be appreciable, thus warranting further *in vitro* and *in vivo* studies. Furthermore, the cuproptosis-related mRNA levels showed no significant increase at the secure concentrations (Figure S11), indicating that the CRNC possessed an appropriate content with controlled copper release.

ROS scavenging and immunoregulation

The antioxidant activities of nanostructures were evaluated. Figure S12a showed that CRNC exhibited superior SOD-like activity. As low as 20 μg/ mL CRNC scavenged 63.2 % of the $O_2^{\cdot-}$ species. Meanwhile, RuO_2-containing nanozymes exhibited excellent CAT-like activity (Figure S12b).

ROS imbalance influences macrophage polarization and is the driving force behind inflammation outbursts, the accumulation will increase oxidative stress in surrounding tissues and aggravate diseases [27]. It was observed that a significantly elevated ROS level existed in macrophages after the exposure of lipopolysaccharide (LPS), while RNC or CRNC treatment would suppress the intracellular ROS (Figure S13a-b); also, a superior efficiency of ROS clearance was found in CRNC behavior by flow cytometry (Figure S13c-d), indicating better cytoprotection against oxidative stress.

Likewise, M1/M2 macrophages reflect the inflammation progress and they participate in immunoregulation by regulating polarization [28]. As depicted in Figure S14a-b, M1-macrophage ($CD86^+$ cell) number had a prominent increase after co-cultural with LPS, accompanied by an up-regulation of pro-inflammatory cytokines (IL-1β, TNF-α, and IL-6) (Figure S14d-f). Notably, $CD206^+$ macrophage percentage as well as anti-inflammation cytokine expressions (IL-10, TGF-β, and Arg-1) was increased after RNC and CRNC treatment (Figure S14b and g-i). Satisfyingly, CRNC exhibited a better performance in promoting M2 polarization. Moreover, immunofluorescence results also demonstrated that the LPS-caused augmented IL-6 and TNF-α expressions were attenuated after RNC or CRNC treatment (Figure S15a-c), matching well with IL-6 secretion in the supernatant (Figure S15d).

Overall, the CRNC-based nanozyme could shift polarization from M1 to M2 by reducing intracellular ROS and down-generating of pro-inflammatory cytokines, which could maintain immune homeostasis and facilitate periodontal regeneration.

In vitro angiogenic and osteogenic effects

Endothelial activity is essential for intact microcirculation and tissue/bone restoration. As illustrated in Fig. 3a-b, the impairment of tubular formation was improved after RNC or CRNC treatment, reflecting an enhanced capillary formation ability. Furthermore, both RNC and CRNC promoted horizontal and vertical migration abilities (Fig. 3c-d and S16a-b). Furthermore, the mRNA (EphB4, VEGF-A, and bFGF) and protein (EphB4 and VEGF-A) levels were remarkably up-regulated by CRNC nanozyme relative to the LPS group (Fig. 3e-f and

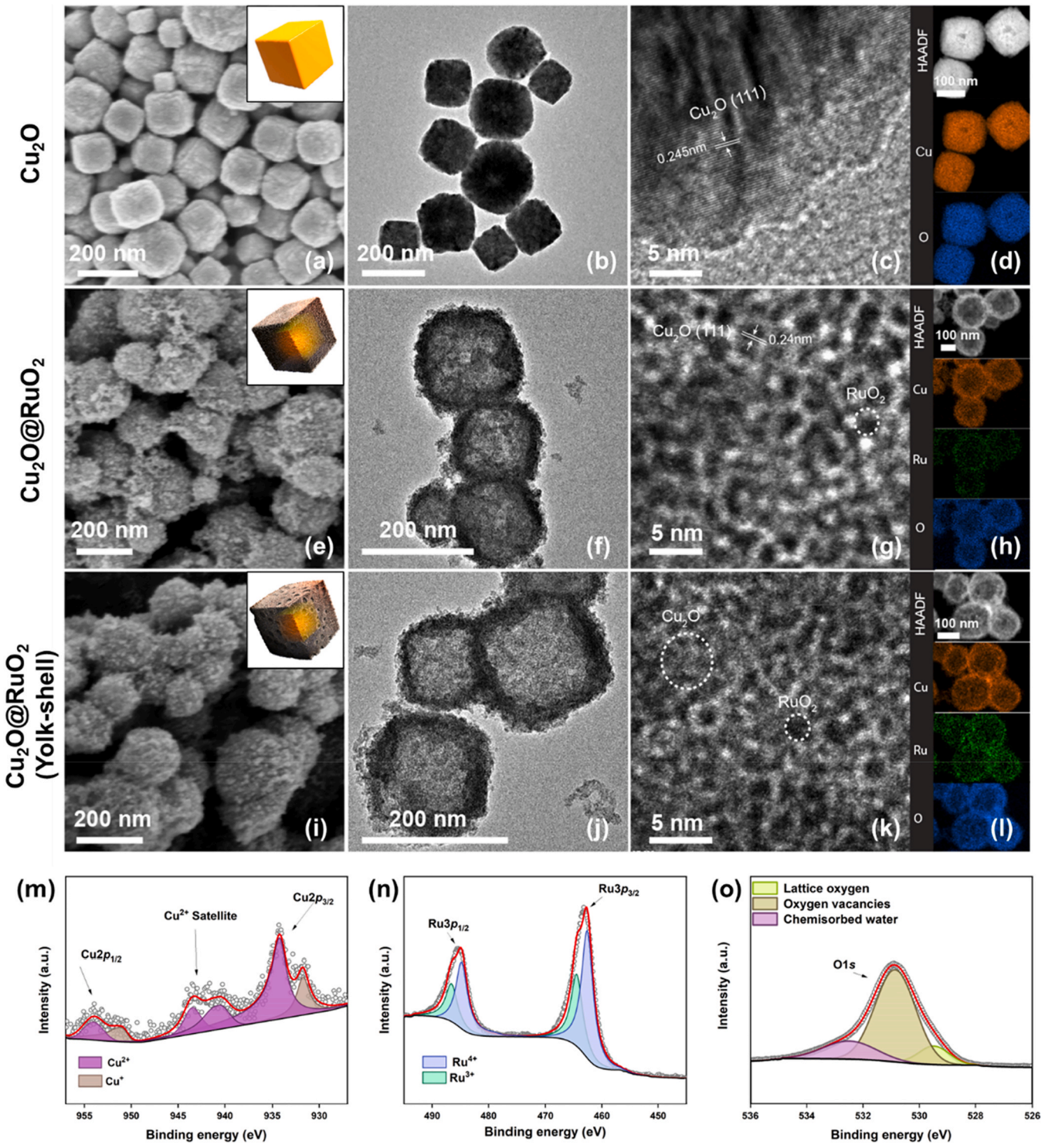

Fig. 2. Structural characterization of CRNC nanozymes. a, e, i) SEM images of Cu_2O, $Cu_2O@RuO_2$, and yolk-shell $Cu_2O@RuO_2$ (scale bar: 200 nm); b, f, j) TEM images of Cu_2O, $Cu_2O@RuO_2$, and yolk-shell $Cu_2O@RuO_2$ (scale bar: 200 nm); c, g, k) HRTEM images of Cu_2O, $Cu_2O@RuO_2$, and yolk-shell $Cu_2O@RuO_2$ (scale bar: 5 nm); and d, h, l) EDX-STEM maps of Cu_2O, $Cu_2O@RuO_2$, and yolk-shell $Cu_2O@RuO_2$. XPS spectra of m) Cu 2*p*, n) Ru 3*p*, and o) O 1 *s* in yolk-shell $Cu_2O@RuO_2$.

S16c-e), consistent with the endothelial biomarker CD31 expression (Figure S17a-b). Vascular healing is mediated through growth factor secretion and metabolic balance [29,30]. The changes in VEGF-A and TNF-α secretions in the supernatant were quantified and results showed the functional recovery, which in turn had a potential impact on the surrounding environment (Figure S17c-d). In addition, Figure S18a-b shows that the expressions of p-ERK1/2, p-JNK, and p-p38 MAPK appreciably increased with CRNC treatment. This implies that CRNC-induced augmentation of angiogenesis improved the tubular formation and endothelial motility, which could provide a driving force behind bone formation.

Moreover, it has been reported that copper-based materials also exhibited a favorable role in osteogenesis through the induction of stem cell differentiation and osteoblastic activation [31,32]. To investigate the osteogenic effect, the activity of alkaline phosphatase (ALP), an early marker of differentiation, was explored [33]. LPS induced an inhibitory

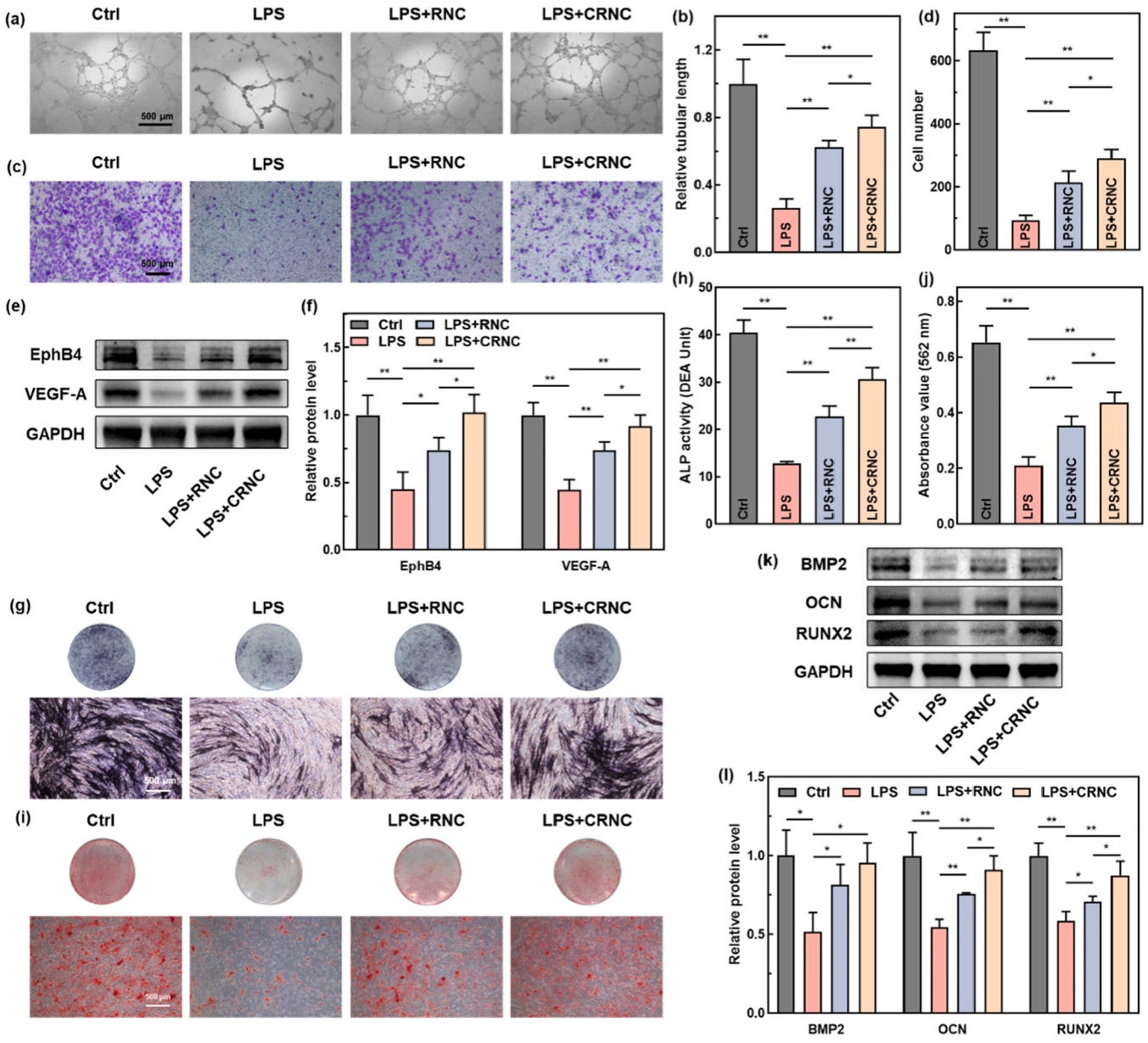

Fig. 3. Angiogenesis and osteogenesis induced by CRNC nanozyme under inflammatory conditions. a) Tubular formation and b) corresponding quantitative data of tubular length with different treatments; c) Transwell assay and d) corresponding quantification of cell number after 24 h incubation in HUVEC. e) Western blot and f) corresponding semi-analysis of angiogenesis-related proteins (EphB4 and VEGF-A). g) ALP staining and h) corresponding ALP activity detection after 14 d of culture; i) ARS staining and j) corresponding quantification of soluble mineralized deposits in PDLSC. k) Western blot and l) corresponding semi-analysis of osteogenesis-related proteins (BMP2, OCN, and RUXN2). RNC or CRNC is 20 μg/mL in HUVEC and 10 μg/mL in PDLSC. Scale bar: 500 μm, $*P < 0.05$, $**P < 0.01$, n = 3.

activity in ALP expression, but the CRNC nanozyme treatment showed a darker ALP staining and superior osteogenic activity (Fig. 3g-h). Concomitantly, alizarin red S (ARS) staining was used to identify mineralized maturation [34]. The tendency of calcium deposition was similar in the presence of LPS after culture for 21 d, whereas the addition of CRNC distinctly increased mineralized nodules (Fig. 3i-j). Notably, the copper incorporation in the nanozyme helped improve the matrix formation of PDLSCs, which elucidated a favorable role of copper in osteogenesis [35]. Osteogenic markers were also detected in gene and protein levels after induction. Remarkably, CRNC displayed superior activity in rescuing the decreased expressions of BMP2, OCN, and RUNX2 under LPS stimulation (Fig. 3k-l and S19a-c). The phosphorylation levels of ERK1/2 and JNK within 12 h following the CRNC treatment are shown in Figure S19d-e. These findings advocated the use of CRNC nanozyme to satisfactorily promote osteoblast differentiation.

As widely reported, favorable vascularization plays an important role in osteogenesis [36]. Therefore, an HUVEC-derived conditional medium was prepared for the osteogenic application. As expected, the conditional medium obtained after LPS treatment showed inhibition in ALP staining, whereas, the addition of CRNC enhanced that expression (Figure S20a). Considering the upregulation of VEGF-A and decline in TNF-α secretions in the supernatant, the low doses (250 ng/mL) of VEGF-A and TNF-α were also explored in osteogenesis to elucidate the possible underlying mechanism (Figure S16f-g). Figure S20b demonstrates that TNF-α effectively suppressed ALP expression, and VEGF-A had a positive influence compared to the control group. These results corroborated an improved anti-inflammatory activity of CRNC and an effective biomineralization due to the responsive release of Cu^{2+}, which

displayed osteogenic properties and indirectly promoted angiogenesis.

Potential mechanisms of angiogenesis and osteogenesis

Having confirmed that CRNC could promote angiogenesis and osteogenesis, the potential mechanisms were explored. Combined with RNA sequencing, Gene Ontology (GO) and Kyoto Encyclopedia of Genes and Genomes (KEGG) analyses were performed to understand gene enrichment (Fig. 4a and S21). Moreover, it was also observed that nanoparticles were located at the cell membrane or plasma, as displayed in the TEM images (Fig. 4b and S22). Taken together, these results implied the involvement of several pathways in the induction of angiogenesis. After the identification of genes and proteins, it can be firmly stated that TGF-β1 and PI3K signals are up-regulated with CRNC incubation under inflammatory conditions (Figure S23a-c), and these proteins play vital roles in nanoparticle-based tissue repair process [37, 38]. To further verify this assumption, small interfering RNA (siRNA) was used to knock down the expression of TGF-β1 (Figure S23d-f) and PI3K (Figure S23g-i) in HUVECs. As a result, significant inhibition in the abilities of horizontal (Figure S24a-b) and vertical (Figure S24c-d) migrations was observed upon silencing of TGF-β1 or PI3K. Particularly, the TGF-β1 knocking down showed a more obvious effect than PI3K in tubular formation (Fig. 4c-d). The effect was also demonstrated in CD31 immunofluorescence and VEGF-A immunoblotting (Fig. 4e and S25a-b), verifying the role of TGF-β in angiogenesis [39]. It should be mentioned that the knocking down of TGF-β1 induced the suppression of PI3K level,

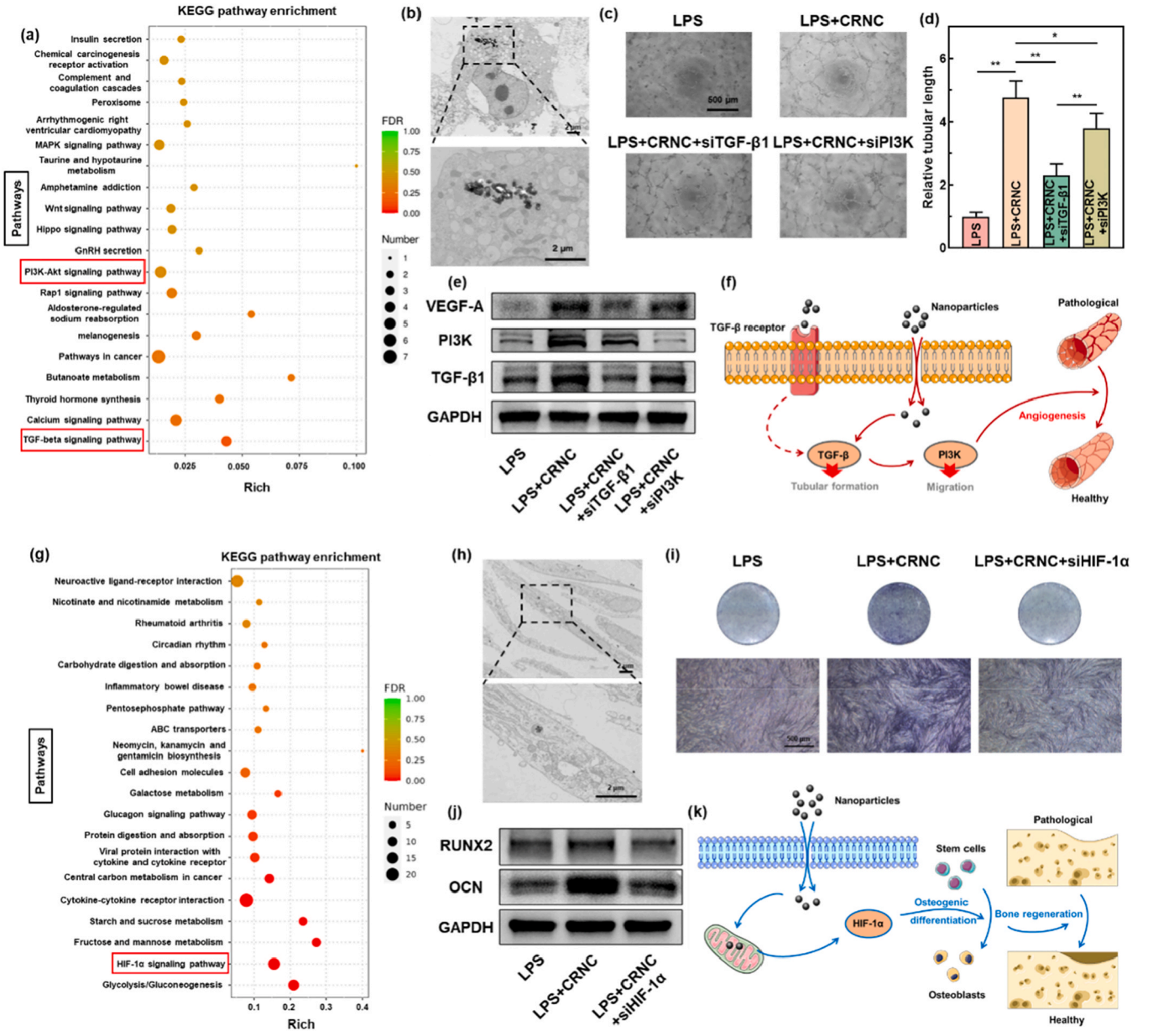

Fig. 4. Potential mechanisms of CRNC nanozyme promoting angiogenesis and osteogenesis. a) KEGG pathway enrichment of HUVECs between LPS and LPS+CRNC groups by RNA sequencing. b) TEM images of HUVECs after material endocytosis for 6 h. Scale bar: 2 μm. c) Tubular formation imaged by microscope and d) corresponding quantification of tubular length. Scale bar: 500 μm, n = 3. e) Immunoblotting of VEGF-A, PI3K, and TGF-β1 after knocking down TGF-β1 or PI3K expression in HUVECs. f) Proposed mechanism of CRNC-induced angiogenesis in HUVECs. g) KEGG pathway enrichment of PDLSCs between LPS and LPS+CRNC groups by RNA sequencing. h) TEM images of PDLSCs after material endocytosis for 6 h (scale bar: 2 μm). i) ALP staining of PDLSCs with indicated treatments (scale bar: 500 μm) and j) immunoblotting of OCN and RUNX2 after knocking down HIF-1α expression in PDLSCs with indicated treatments. k) Proposed mechanism of CRNC-induced osteogenesis in PDLSCs. CRNC is 20 μg/mL in HUVEC and 10 μg/mL in PDLSC. *$P < 0.05$, * * $P < 0.01$.

but PI3K silencing could not inhibit the expression of TGF-β1, implying that CRNC-provoked PI3K up-regulation originally originated from TGF-β (Fig. 4e and S25c). Also, TGF-β receptor (TGFβR) inhibitor (SB431542) was utilized to make further confirmation. The immunoblotting results showed that the application of SB431542 could fairly suppress elevated expressions of TGF-β1, PI3K, and VEGF-A induced by CRNC (Figure S26), thus proving the relationship between TGF-β and PI3K. These findings suggested that CRNC could not only enter the cytoplasm but also bind with membrane receptors, promoting the angiogenesis of HUVECs through the activation of the TGF-β/PI3K pathway (Fig. 4f). To investigate whether the TGF-β or PI3K activation was specific to CRNC, RNC was used as a control. PI3K pathway was activated with RNC exposure, whereas no difference was noticed in TGF-β1 (Figure S27a-b). Moreover, it was found that blocking PI3K had an inhibitory effect on cell migration (Figure S27c-f) but exerted no significant effect on tubular formation (Figure S27g-h). It is worth noting that the TGF-β activation triggered by CRNC was not observed when treated with RNC, which suggested that Cu^{2+} released from CRNC is a meaningful stimulus to drive TGF-β-induced angiogenesis [40].

Similarly, RNA-seq was conducted in PDLSCs after CRNC treatment. Much higher signals were detected in the extracellular matrix and oxygen level response (Fig. 4g and S28). Following endocytosis, CRNC were colocalized in mitochondria (Fig. 4h and S29). Following the identification of gene and protein levels, the hypoxia-inducible factor 1α (HIF-1α) pathway was reasonably engaged in the osteogenic process (Figure S30a-c). Afterward, siRNA of HIF-1α was constructed (Figure S30d-f). ALP staining displayed much weaker intensity with suppressed expressions of RUNX2 and OCN compared to the LPS+CRNC group (Fig. 4i-j and S30g), indicating a declined osteogenic differentiation activity when HIF-1α was knocked down. These findings implied that CRNC could accelerate bone regeneration by facilitating osteogenic differentiation of PDLSCs via the HIF-1α signal under inflammatory conditions (Fig. 4k). Notably, it was revealed that HIF-1α could also be up-regulated by RNC (Figure S31a-b). With the blocking of HIF-1α level, ALP activity was also inhibited (Figure S31c), demonstrating both RNC and CRNC were responsible for osteogenic differentiation through HIF-1α pathway.

The above multiple results demonstrated that CRNC displayed better performance compared to RNC under the same concentration, which is likely due to better engagement of CRNC in both angiogenesis and osteogenesis. To further clarify the mechanism, a higher concentration of RNC was used to further downregulate the mRNA levels of IL-1β and TNF-α to achieve similar anti-inflammation activity to CRNC (Figures S14d-e and S32a-b). Moreover, preferable tube images (Figure S32c-d) and slightly darker ALP staining were shown in CRNC compared to the RNC group (Figure S32e), which proved the crucial and favorable roles of Cu^{2+} in angiogenesis and osteogenesis.

Overall, the CRNC nanozyme exhibited multiple desirable features, including anti-inflammation, osteogenesis, and angiogenesis. Through introducing a smart copper reservoir, CRNC induced a preferable angiogenic activity via TGF-β/PI3K activation and promoted osteogenic differentiation via the activation of HIF-1α signaling pathway.

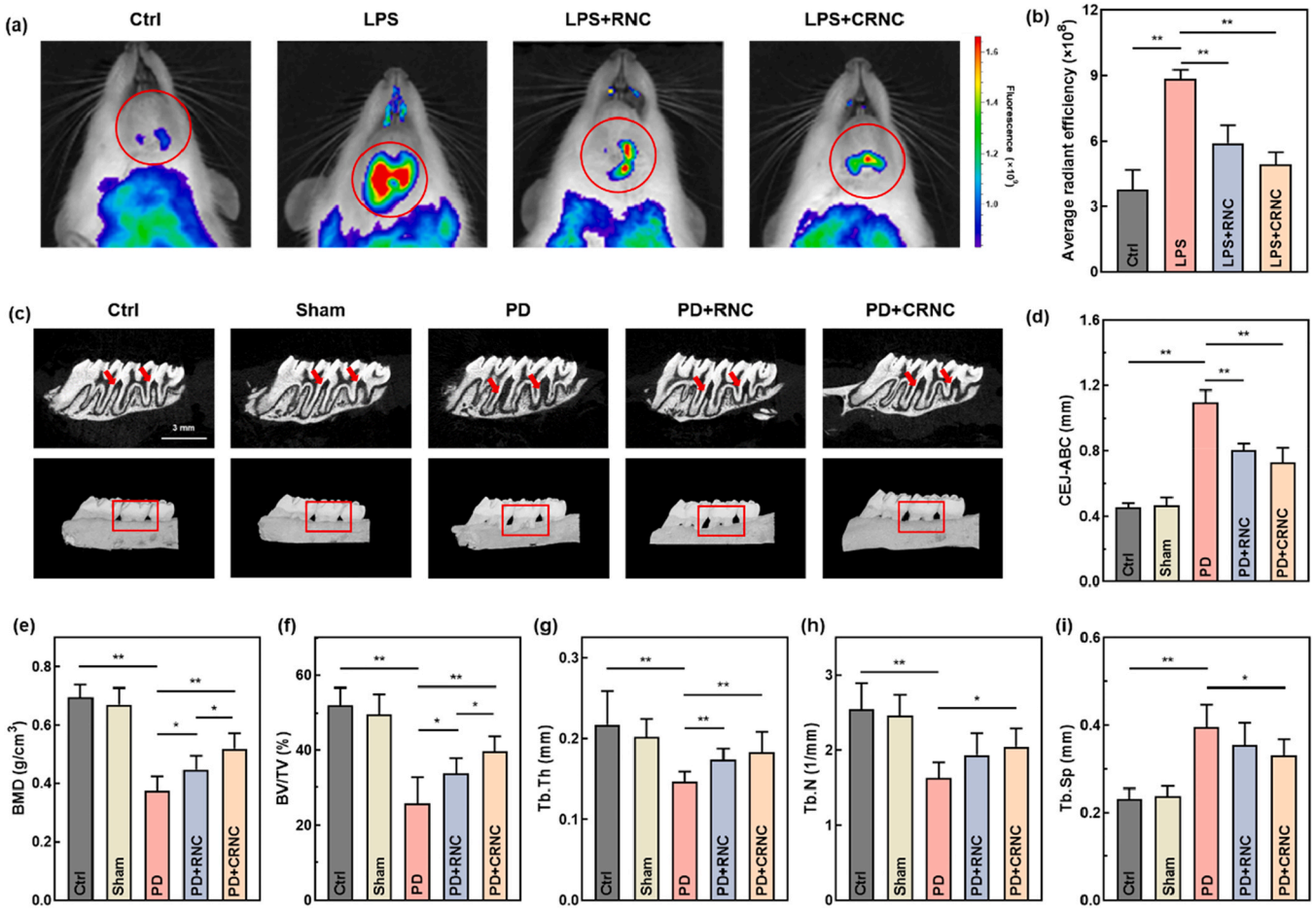

Fig. 5. Effects of CRNC on periodontal inflammation and bone regeneration *in vivo*. a) *In vivo* fluorescence and b) quantification of ROS level at the site of periodontal inflammation after treatments (n = 3). c) 3D micro-CT construction of maxilla (scale bar: 3 mm) and analyses of alveolar parameters for d) CEJ-ABC, e) BMD, f) BV/TV, g) Tb. Th, h) Tb. N, and i) Tb. Sp after different therapies in periodontitis model (n = 6). Red circles indicate the probe region; red arrows indicate mesial and distal alveolar crests; red squares indicate the ligated second molars. *$P < 0.05$, * * $P < 0.01$.

In vivo periodontitis therapy by CRNC

Encouraged by the anti-inflammatory, angiogenic, and osteogenic activities of CRNC, we explored the potential of CRNC for ameliorating inflammation and inducing periodontal regeneration *in vivo*. Fig. 5a-b shows that the LPS-induced group exhibited the strongest fluorescence; most of the ROS signals originated from the gingival site. Upon treatment with CRNC, a marked reduction in ROS level was achieved due to its biocatalytic and anti-inflammatory properties (red circles), displaying its potential to diminish inflammation and lay the foundation for periodontal regeneration [41]. Subsequently, periodontitis model was established to evaluate alveolar regeneration. After 4 weeks of treatment, the rats were sacrificed and the maxillary samples were scanned for micro-CT analysis and 3D reconstruction (Fig. 5c). The second molars (red arrows and frames) were chosen for the measurement from the cemento enamel junction (CEJ) to the apex of the alveolar bone crest (ABC). A higher CEJ-ABC value was observed after ligation in the periodontitis (PD) group. In contrast, CRNC intervention helped to reduce that distance (Fig. 5d). To further determine the therapeutic efficacy, the bone parameters including bone mineralized density (BMD, g/cm^3), bone volume fraction (bone volume/tissue volume, BV/TV, %) and trabecular thickness (Tb. Th, mm), trabecular number (Tb. N, 1/mm), and trabecular separation (Tb. Sp, mm) were evaluated (Fig. 5e-i). PD group showed significant changes, with 46 % reduction in BMD, 50.3 % in BV/TV, 32.6 % in Tb. Th, 36.4 % in Tb. N, 71 % increase in Tb. Sp value, compared to the control group, indicating the successful construction of the periodontitis model [42]. Following the treatment with RNC or CRNC, higher values of BMD, BV/TV, Tb. Th, and Tb. N, as well as a lower value in Tb. Sp were noticed, demonstrating a remarkable therapeutic efficacy of both RuO_2-based nanozymes. Furthermore, CRNC showed a reinforced activity for bone regeneration relative to RNC, suggesting that CRNC could prominently accelerate alveolar regeneration.

Histological and immunological stainings

To further affirm the above results, histological and immunological stainings were performed. The alveolar outline (black lines) could be observed in hematoxylin and eosin (H&E) staining. PD group showed severe bone absorption with elevated inflammatory cell infiltration (Fig. 6a); on the contrary, the destroyed bone was repaired with fewer immune cell infiltration in the CRNC group because of its excellent ROS scavenging and angiogenic abilities.

A delicate balance between osteoblast and osteoclast is required for bone absorption and reconstruction [14]. Hence, Trap staining was conducted to evaluate osteoclast activity. As shown in Fig. 6b-c, the number of osteoclasts (red arrows) was calculated. Compared to the PD group, a pronounced drop in the number of osteoclasts was detected in the CRNC treatment group, indicating reduced bone loss. Moreover, the organized and dense collagen fibers were degraded and arranged in a disorderly manner in PD (can be seen as red-stained areas). The CRNC treatment could stimulate collagen type I expression (Figure S33a), which is beneficial to osseous mineralization [43]. In addition, Goldner's trichrome staining was employed and the deep green region demonstrated a high degree of mineralization around the teeth [44]. It was apparent in Fig. 6d that CRNC induced more bone mineralization than the RNC group due to the presence of a smart copper reservoir. Finally, inflammation marker TNF-α (Figure S33b-c) and osteogenesis marker OCN were evaluated (Fig. 6e-f). According to the analysis of integrated optical density (IOD), the CRNC exposure induced the down-regulation of TNF-α and up-regulation of OCN, compared to the PD group, suggesting a successful periodontal regeneration.

The integration of copper with antioxidant RuO_2 nanozyme helped achieve a better impact on inflammation remission, osteogenesis, and angiogenesis *in vitro* and effectively improved bone regeneration in PD. Furthermore, ventralis blood vessels were isolated and cultured *ex vivo* with corresponding treatments (Figure S34a). LPS caused endothelial

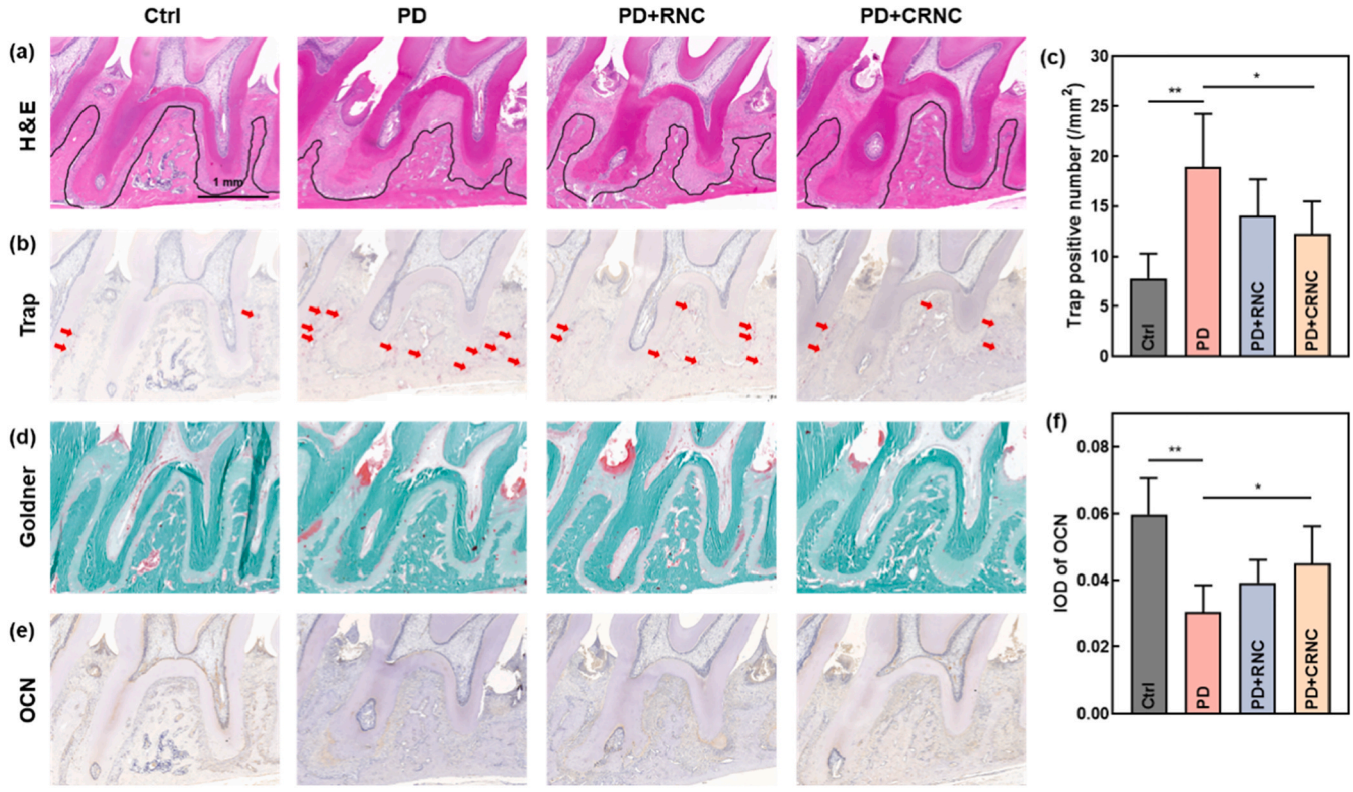

Fig. 6. *In vivo* evaluation of anti-inflammation and osteogenesis in the maxilla. a) H&E staining. Black lines indicate the alveolar morphology. b) Trap staining and (c) enumeration of osteoclasts. Red arrows point to the osteoclasts. d) Goldner's trichrome staining. e) Immunohistochemical staining of OCN and f) corresponding semi-analysis. Scale bar= 1 mm. Scale bar: 1 mm, $^*P < 0.05$, $^{**}P < 0.01$, n = 6.

debonding and reduced collagen expression, whereas the intervention of CRNC could help relieve the problems (Figure S34b-c). VEGF-A expression in the endothelium showed an ascending trend in CRNC, compared to the LPS group (Figure S34d-e). Collectively, the above observations implied that CRNC would maintain vascular homeostasis under inflammatory conditions. Additionally, to assess the biosafety, the main organs including the heart, liver, spleen, lung, and kidney were sectioned for H&E staining (Figure S35). No abnormality was observed, indicating that RNC and CRNC have good biocompatibility for *in vivo* therapy.

Conclusion

Most of the reported antioxidant nanozymes focused on anti-inflammatory and osteogenic activities for periodontitis treatment (Table S1), however, effective periodontal regeneration also requires angiogenesis. In this study, we designed a smart copper ion-releasing yolk-shell nanozyme, comprised of a porous RuO_2-coated Cu_2O. The developed nanozyme was capable of releasing copper ions under inflammatory stimulation and exhibited multiple functions: the RuO_2 participated in modulating inflammation by scavenging ROS and inducing macrophage polarization. The released copper ions realized an enhanced periodontal regeneration through angiogenesis and osteogenesis. We elucidated the underlying mechanisms responsible for the induction of angiogenesis and osteogenesis. The *in vitro* results demonstrated the role of the TGF-β/PI3K pathway in nanozyme-induced angiogenesis, whereas the osteogenic differentiation was associated with the HIF-1α signaling pathway. When applied in an *in vivo* model, CRNC displayed decent bone regeneration in PD. Overall, it is envisioned that such a rationally designed nanozyme will provide a new strategy for developing nanomedicines based on guided bone regeneration.

Materials and methods

Chemicals and reagents

Ruthenium chloride hydrate ($RuCl_3{\cdot}xH_2O$), polyvinylpyrrolidone (PVP, MW ~40000), copper nitrate trihydrate ($Cu(NO_3)_2{\cdot}3H_2O$), ethylene glycol (EG), sodium hydroxide (NaOH), and nitric acid 65 % (HNO_3) were purchased from Aladdin Chemical Co. Ltd. (Shanghai, China). All other reagents and chemicals were purchased from commercial sources and used as received. Deionized water (18.2 MΩ·cm, Millipore) and absolute ethanol were used throughout the experiments. The primer sequences are listed in Table S2 and detailed information on antibodies is given in Table S3.

Instrumentation

The structural characteristics of the materials were studied using a scanning electron microscope Ultra 55 (Zeiss, Germany) and a TEM equipment (FEI TECNAI G2 F20) operated at 200 kV. HAADF-STEM imaging was carried out using an aberration-corrected STEM Titan Cubed G2 300 system. A diffractometer (Bruker-AXS, Germany) with Cu Kα radiation was used to collect powder XRD patterns. The elemental compositions were determined by an inductively coupled plasma optical emission spectrometer (Avio 220 Max, PerkinElmer). XPS analysis was done by a Thermo Scientific K-Alpha spectrometer (Al Kα (1486 eV) using a hemispherical energy analyzer; the binding energy was calibrated using C1*s* at 284.8 eV. Zeta potentials were determined at 25 °C using a Malvern Zetasizer Nano ZS90. The Brunauer-Emmett-Teller (BET) surface areas were obtained at 77 K on a Kubo X1000 (Biaode, China) and calculated using N_2 adsorption-desorption isotherms.

Synthesis of Cu_2O nanocubes

In a typical procedure, 600 mg of PVP and 2 mmol of copper nitrate trihydrate were dissolved in 50 mL of water-free ethylene glycol [45]. Then, the solution was heated to 185 °C under vigorous magnetic stirring and maintained for 60 min. The resulting orange-colored product was collected by centrifugation and washed thrice with ethanol and distilled water.

Synthesis of $Cu_2O@RuO_2$ core-shell nanocubes

One milliliter of an aqueous solution of $RuCl_3.xH_2O$ (75 mg) was introduced into a 10 mL aqueous solution of the as-synthesized Cu_2O (50 mg) under vigorous stirring at room temperature to spontaneously grow a shell of ultrasmall RuO_2 nanoparticles. After 30 min stirring, the solution was centrifuged to recover the product; the obtained product was then redispersed in 20 mL of water, and adjusted the pH of the solution to 10 under stirring. Afterward, the solution was heated at 80 °C for 30 min to improve the quality of the RuO_2. Subsequently, the core-shell-like nanostructure was recovered via centrifugation and washed with water.

Synthesis of CRNC

To etch the Cu_2O core, the $Cu_2O@RuO_2$ nanocubes were treated with nitric acid. 30 mg $Cu_2O@RuO_2$ nanocubes were dispersed in deionized water (20 mL) and then the diluted solution of 10 μL concentrated HNO_3 was slowly added under stirring. After one hour of incubation in an acidic medium, the final CRNC was collected via centrifugation and washed with water and ethanol.

Synthesis of hollow RNC

To completely etch the Cu_2O core, the $Cu_2O@RuO_2$ nanocubes were also treated with nitric acid. 30 mg core-shell nanocubes of $Cu_2O@RuO_2$ were dispersed in deionized water (20 mL) and then the diluted solution of 30 μL concentrated HNO_3 was slowly added under stirring. After one hour of incubation in an acidic medium, the final RNC was collected via centrifugation and washed with water and ethanol.

SOD-like activity

The SOD-like activity was measured by SOD kits (Dojindo, Japan) according to the reduction reaction of WST-1 by O_2^-. The samples were added into the solutions containing working buffer and measured at an absorbance of 450 nm after culture for 20 min.

CAT-like activity

The CAT-like activity was measured using CAT kits (Beyotime, China) considering the consumption of H_2O_2 and generation of O_2. After preparation and incubation for 30 min, the samples were measured at an absorbance of 520 nm.

Cell culture and treatment

PDLSCs were obtained from premolar extractions by 5 volunteers during the orthodontic treatment, as reported in previous work [14]. PDLSCs and macrophage cell line RAW264.7 were cultured in Dulbecco's modified eagle medium (DMEM, Gibco, USA) with 10 % fetal bovine serum (FEB, Gibco) and 1 % penicillin and streptomycin. HUVECs were cultured in an endothelial cell medium (ECM, ScienCell, USA) containing 5 % FBS, 1 % penicillin and streptomycin, and 1 % endothelial cell growth supplement.

Cell viability

RAW264.7 cells, HUVECs, and PDLSCs were seeded in 96-well plates at the density of 5×10^3 per well and treated with different concentrations of RNC or CRNC. After culture for different times, cells were washed with PBS and incubated with a medium containing Cell Counting Kit-8 (CCK-8, Dojindo). Afterward, the absorbance was measured at 450 nm using a microplate reader. Three kinds of cells were seeded in 6-well plates and treated with CRNC. After a corresponding time, total RNA was extracted with RNA isolation kits (Vazyme, China), and reverse transcription was conducted using the HiScript III cDNA synthesis kit (Vazyme). Finally, RT-qPCR was carried out using a SYBR Mix kit (AG11735, Accurate Biotechnology (Hunan), China) for the detection of ATP7A and FDX1. The expression levels of genes were calculated by the $2^{-\Delta\Delta Ct}$ method.

Anti-inflammation property

RAW264.7 cells were cultured in a 12-well plate at a density of 5×10^4/well with 250 ng/mL lipopolysaccharide (LPS, Sigma, USA) and treated with RNC or CRNC (20 μg/mL) for 24 h, and then cells were washed with PBS and incubated with DCFH-DA probes (Beyotime). Next, the intracellular ROS was measured by flow cytometry (BD Biosciences, USA) and observed under a confocal laser scanning microscopy (CLSM).

Macrophage polarization was determined by cell surface markers and gene expression. RAW264.7 cells were seeded in 6-well plates with 250 ng/mL LPS and nanozymes for 24 h. Then, cells were collected for incubation with CD86/CD206 and detected by flow cytometry. RT-qPCR was conducted to investigate the expressions of M1 biomarkers (IL-1β, TNF-α, IL-6) and M2 biomarkers (IL-10, TGF-β, Arg-1). Additionally, the protein levels of TNF-α and IL-6 were detected by immunofluorescence. After being fixed with 4 % paraformaldehyde and blocked with 5 % BSA, cells were incubated with primary antibodies at 4 °C overnight, respectively. Afterwards, the labeled secondary antibodies were added and DAPI staining was conducted, followed by CLSM observation. Finally, an enzyme-linked immunosorbent assay (ELISA) was performed to assess IL-6 secretion in the suspension by the immunological kits (Elabscience, China).

Angiogenic activity

HUVECs were seeded in 6-well plates and pretreated with LPS (10 μg/mL) and nanozymes for 3 d. Subsequently, pipette tips were used to make parallel scratches after cell conjugation, medium with free FBS was added into each well, and then cell migration areas were analyzed 24 h later. The transwell assay was conducted using 24-well transwell chambers with polycarbonate membranes (8 μm pore). After pretreatments, HUVECs were seeded in the upper chambers, and a medium with 10 % FBS was added into the lower chambers. One day later, the cells were fixed with 4 % paraformaldehyde and stained with 0.1 % crystal violet. The number of migrating cells from the upper surface was quantified. For tubular formation, the pretreated cells were collected and seeded in a Matrigel-coated 96-well plate (BD Bioscience) at a density of 1.5×10^4/well, and cultured under different treatments at 37°C. Tubular structures in the Matrigel were observed with an optical microscope and the length of the tubules was quantified.

HUVECs were seeded in 6-well plates and treated with LPS (10 μg/mL), nanozymes, or SB431542 (5 μM, MCE, USA) for different times. Then, RT-qPCR was conducted to examine the gene expressions of EphB4, VEGF-A, and bFGF. Meanwhile, the protein levels of EphB4 and VEGF-A and the phosphorylation levels of ERK1/2, JNK, and p38 MAPK were determined by western blot. Total proteins were extracted with RIPA buffer (ThermoFisher, USA), electrophoresed and separated on 4–20 % SDS-PAGE gels, and transferred onto PVDF membranes. Afterward, the membranes were blocked and incubated with primary antibodies at 4 °C overnight. After washing in TBST, the membranes were treated with the secondary antibody and visualized using a chemiluminescence reagent (Vazyme). In addition, immunofluorescence was conducted to observe CD31 expression in HUVECs, and ELISA kits were used to detect the TNF-α (Multisciences, China) and VEGF-A (Elabscience) secretions in the suspension.

Osteogenic differentiation activity

The osteogenic differentiation medium (containing 0.1 μm dexamethasone, 10 mM β- glycerophosphate, and 50 mM ascorbic acid) was prepared for PDLSCs culture. For ALP detection, PDLSCs were seeded in 24-well plates with different treatments and the medium was replaced every 3 days. Then, ALP staining was performed using the NBT/BCIP kit (Beyotime), and the quantity was determined by the ALP activity Kit (Beyotime). For ARS, the mineralized depositions were stained using an OriCell® ARS solution (Cyagen (Guangzhou), China). Subsequently, ARS was quantified by dissolving the stained depositions in 10 % (w/v) cetylpyridinium chloride and the absorbance was measured at 562 nm using a microplate reader.

PDLSCs were seeded in 6-well plates and cultured with LPS (10 μg/mL) and nanozymes for different times, RT-qPCR was conducted to examine the gene expressions of BMP2, OCN, and RUNX2. Also, the protein level of BMP2, OCN, and RUNX2 and phosphorylation levels of ERK1/2 and JNK were confirmed by western blot.

Co-culture system of angiogenesis and osteogenesis

After cultured with 10 μg/mL LPS and 20 μg/mL RNC or CRNC, new DMEM with free FBS medium was replaced into HUVECs for 2 d. Then, cell suspensions were collected, centrifuged, and filtrated to remove the impurity. Subsequently, the conditional medium was prepared by mixing HUVEC-derived medium and osteogenic differentiation medium at a ratio of 1:1 for osteogenic induction. PDLSCs were seeded in a 24-well plate and induced with a conditional medium. Seven days later, ALP staining was conducted to investigate the osteogenic differentiation.

TEM observation

HUVEC and PDLSC samples were fixed in 2.5 % glutaraldehyde and 1 % osmic acid orderly. With the subsequent dehydration in gradient alcohol and embedding, the samples were sectioned and stained in 2 % uranyl acetate and 2.6 % lead citrate successively. Finally, the morphological structures were observed using a TEM microscope.

Transcriptome analysis

Total RNA was isolated using the Trizol Reagent (Invitrogen) from the samples treated with LPS (10 μg/mL) and CRNC (HUVEC: 20 μg/mL; PDLSC: 10 μg/mL); cDNA was synthesized using random oligonucleotides. The sequencing libraries were generated by the following steps of cDNA synthesis and purification. Then, the library was sequenced on a Bioanalyzer 2100 system (PANOMIX Biomedical Tech Co., LTD, China). Different expression of genes was analyzed by DESeq (1.30.0), the screening conditions are as follows: expression difference multiple $|\log2FoldChange| > 1$, significant P-value < 0.05. Using topGO to perform GO enrichment analysis on the differential genes and ClusterProfiler (3.4.4) software was used to carry out the enrichment analysis of the KEGG pathway of differential genes.

siRNA transfection

After the confirmation of potential targets, gene silencing was used to conduct the biological mechanisms. Cells were cultured and seeded in 6-well plates. The siRNA (Synthbio, China) was mixed with lipofectamine2000 (Thermo Fisher Scientific, USA) in serum-free medium for

20 min at room temperature, then the mixture was added in the plate for 24 h, and the cells were treated for the following assays.

To determine the transfection, total RNA and proteins were extracted for RT-qPCR and western blot to identify the gene silencing.

Animal experiments

The experiments were performed under specific pathogen-free conditions according to the "Guidelines for the Ethical Review of Laboratory Animal Welfare".

LPS and nanozymes were injected into the region of alveolar mucosa in mandible anterior teeth of Sprague-Dawley (SD) rats (SPF Biotechnology, China) for 3 d and 1 d, respectively. After that, DCFH-DA was added to the same site and ROS signals were examined using an imaging instrument (PE, Spectrum, USA).

For *ex vivo* blood vessel culture, sixteen SD rats were sacrificed and the blood vessels of the ventralis aorta were separated, detached, and clipped. The blood vessels were challenged with the stimulations for 7 d and the tissues were fixed in 4 % paraformaldehyde for histology and immunological staining.

To establish the periodontitis model, a diameter of 0.2 mm ligature wire was tied surrounding the second molar in the maxilla after SD rats were anesthetized. Saline (25 μL) and RNC or CRNC were injected into the submucoperiosteum of the alveolar crest surrounding the second molars every three days. Rats were randomly divided into five groups: 1) Blank control (Healthy rats without periodontitis), 2) Sham group (the ligature wire was tied and loosened immediately), 3) Periodontitis group (PD; Periodontitis without treatment), 4) Periodontitis treated with RNC, 5) Periodontitis treated with CRNC. After 4 weeks, the rats were sacrificed, and then the maxillae and viscera were collected and fixed in 4 % paraformaldehyde. Maxillae were prepared for micro-CT analysis to examine the indexes of the distance from cementoenamel junction (CEJ, mm) to the apex of the alveolar bone crest (ABC), bone volume fraction (bone volume/tissue volume, BV/TV, %) and trabecular thickness (Tb. Th, mm), trabecular number (Tb. N, 1/mm) and trabecular separation (Tb. Sp, mm).

The blood vessel, maxillae, and viscera samples were embedded after dehydration. Next, sections were made and histological stainings including H&E staining, Masson staining, trap staining, and Goldner staining were performed. Immunological stainings (IHC) for OCN and TNF-α were performed. Finally, the results were observed with a microscope and analyzed using ImageJ software.

Statistical analysis

All data were presented as the mean ± standard deviation and analyzed using the SPSS software (IBM, USA) by one-way analysis of variance, and $^{*}P < 0.05$, $^{**}P < 0.01$ was considered to be statistically significant.

CRediT authorship contribution statement

Yuyang Li: Formal analysis, Funding acquisition, Investigation, Methodology, Writing – original draft. **Faheem Muhammad**: Investigation, Methodology, Writing – original draft. **Xiwen Chen**: Formal analysis, Investigation, Methodology, Software, Writing – review & editing. **Deao Gu**: Data curation, Investigation, Software. **Wen Li**: Funding acquisition, Investigation. **Jiayi Tang**: Data curation, Formal analysis. **Mingyue Cheng**: Data curation, Formal analysis. **Jiang Du**: Formal analysis, Methodology. **Shuwei Qiao**: Data curation, Investigation. **Yu Deng**: Methodology, Validation. **Qing Yu**: Methodology, Visualization. **Hui Wei**: Funding acquisition, Project administration, Supervision, Writing – review & editing. **Leiying Miao**: Funding acquisition, Project administration, Supervision, Writing – review & editing.

Declaration of Competing Interest

The authors declare no competing interests.

Acknowledgments

This work was supported by the National Natural Science Foundation of China (22374071, by H. W.), Jiangsu Provincial Key R&D Program (BE2022836, by H. W.), Natural Science Foundation of Jiangsu Province (BK20221177, by L. M.), "2015" Cultivation Program for Reserve Talents for Academic Leaders of Nanjing Stomatological School, Medical School of Nanjing (0223A203, by L. M.), Postgraduate Research & Practice Innovation Program of Jiangsu Province (KYCX23_0192, by Y. L.; SJCX24_0009, by W. L.) and Nanjing Department of Health (YKK23183, by W. L.; ZKX24056, by L. M.).

Appendix A. Supporting information

Supplementary data associated with this article can be found in the online version at doi:10.1016/j.nantod.2024.102624.

Data availability

Data will be made available on request.

References

[1] R.J. Genco, M. Sanz, Periodontology 2000 83 (2020) 7–13.
[2] H. Zhang, T. Xu, Y. Wei, N. Wei, Z. Han, W. Hu, J. Clin. Periodontol (2024).
[3] D. Herrera, M. Sanz, M. Kebschull, S. Jepsen, A. Sculean, T. Berglundh, P. N. Papapanou, I. Chapple, M.S. Tonetti, E.F.P.W. Participants, C. Methodological, J. Clin. Periodontol 49 (24) (2022) 4–71.
[4] M. Yamamoto, R. Aizawa, Periodontology 2000 86 (2021) 142–156.
[5] X. Xin, J. Liu, X. Liu, Y. Xin, Y. Hou, X. Xiang, Y. Deng, B. Yang, W. Yu, ACS Nano 18 (2024) 8307–8324.
[6] J.D. Hathaway-Schrader, C.M. Novince, Periodontology 2000 86 (2021) 157–187.
[7] J. Wu, X. Wang, Q. Wang, Z. Lou, S. Li, Y. Zhu, L. Qin, H. Wei, Chem. Soc. Rev. 48 (2019) 1004–1076.
[8] H. Fan, R. Zhang, K. Fan, L. Gao, X. Yan, ACS Nano 18 (2024) 2533–2540.
[9] I. Zare, D. Choi, J.Y. Zhang, M.T. Yaraki, A. Ghaee, S.Z. Nasab, R. Taheri-Ledari, A. Maleki, A. Rahi, K.L. Fan, J. Lee, Nano Today 56 (2024) 102276.
[10] Y.H. Zhang, G. Wei, W.L. Liu, T. Li, Y.T. Wang, M. Zhou, Y.F. Liu, X.Y. Wang, H. Wei, Nat. Rev. Method Prime 4 (2024).
[11] P. Jiang, L. Zhang, X. Liu, C. Ye, P. Zhu, T. Tan, D. Wang, Y. Wang, Nat. Commun. 15 (2024) 1010.
[12] W. Gao, J. He, L. Chen, X. Meng, Y. Ma, L. Cheng, K. Tu, X. Gao, C. Liu, M. Zhang, K. Fan, D.W. Pang, X. Yan, Nat. Commun. 14 (2023) 160.
[13] Y. Sun, S. Mu, Z. Xing, J. Guo, Z. Wu, F. Yu, M. Bai, X. Han, C. Cheng, L. Ye, Adv. Mater. 34 (2022) e2206208.
[14] B. Zhu, J. Wu, T. Li, S. Liu, J. Guo, Y. Yu, X. Qiu, Y. Zhao, H. Peng, J. Zhang, L. Miao, H. Wei, Adv. Health Mater. 13 (2024) e2302485.
[15] H.P. Gerber, T.H. Vu, A.M. Ryan, J. Kowalski, Z. Werb, N. Ferrara, Nat. Med 5 (1999) 623–628.
[16] Q. Qin, S. Lee, N. Patel, K. Walden, M. Gomez-Salazar, B. Levi, A.W. James, Exp. Mol. Med 54 (2022) 1844–1849.
[17] Y. Li, Y. Zhao, L. Song, L. Xiong, W. Li, W. Wu, L. Miao, J. Periodontal Res. 58 (2023) 225–236.
[18] M. Xie, Q. Tang, J. Nie, C. Zhang, X. Zhou, S. Yu, J. Sun, X. Cheng, N. Dong, Y. Hu, L. Chen, Circ. Res. 126 (2020) e15-e29.
[19] T. Liu, B. Xiao, F. Xiang, J. Tan, Z. Chen, X. Zhang, C. Wu, Z. Mao, G. Luo, X. Chen, J. Deng, Nat. Commun. 11 (2020) 2788.
[20] S. Xu, Q. Wu, B. He, J. Rao, D.H.K. Chow, J. Xu, X. Wang, Y. Sun, C. Ning, K. Dai, Biomaterials 288 (2022) 121751.
[21] T. Tsang, C.I. Davis, D.C. Brady, Curr. Biol. 31 (2021) R421–R427.
[22] R. Zhang, G. Jiang, Q. Gao, X. Wang, Y. Wang, X. Xu, W. Yan, H. Shen, Nanoscale 13 (2021) 15937–15951.
[23] F. Muhammad, X.W. Chen, J.Y. Tang, Y. Cheng, Y.Y. Li, C.X. Zhu, Y.H. Zhang, L. Y. Miao, Y. Deng, H. Wei, Chem. Sci. 15 (2024) 1679–1691.
[24] D. Choi, H. Jung, J. Im, S.Y. Yi, S. Kim, D. Lee, S. Park, C. Lee, J. Kim, J.W. Han, J. Lee, Adv. Mater. 36 (2024) e2306602.
[25] Y.J. Zhang, W.H. Gao, Y.A. Ma, L.L. Cheng, L. Zhang, Q.G. Liu, J.Y. Chen, Y. R. Zhao, K.S. Tu, M.Z. Zhang, C. Liu, Nano Today 49 (2023) 101768.
[26] R.D. Kent, P.J. Vikesland, Environ. Sci. Technol. 50 (2016) 6772–6781.
[27] M. Pu, H. Cao, H. Zhang, T. Wang, Y. Li, S. Xiao, Z. Gu, Mater. Horiz. 11 (2024) 3721–3746.
[28] S. Butenko, R.R. Nagalla, C.F. Guerrero-Juarez, F. Palomba, L.M. David, R. Q. Nguyen, D. Gay, A.A. Almet, M.A. Digman, Q. Nie, P.O. Scumpia, M.V. Plikus, W.F. Liu, Nat. Commun. 15 (2024) 6820.

[29] H. Bi, H. Li, C. Zhang, Y. Mao, F. Nie, Y. Xing, W. Sha, X. Wang, D.M. Irwin, H. Tan, Stem Cell Res. Ther. 10 (2019) 302.
[30] U.H. Langen, M.E. Pitulescu, J.M. Kim, R. Enriquez-Gasca, K.K. Sivaraj, A. P. Kusumbe, A. Singh, J. Di Russo, M.G. Bixel, B. Zhou, L. Sorokin, J.M. Vaquerizas, R.H. Adams, Nat. Cell Biol. 19 (2017) 189–201.
[31] I. Burghardt, F. Luthen, C. Prinz, B. Kreikemeyer, C. Zietz, H.G. Neumann, J. Rychly, Biomaterials 44 (2015) 36–44.
[32] X. Qu, Z. He, H. Qiao, Z. Zhai, Z. Mao, Z. Yu, K. Dai, J. Orthop. Transl. 14 (2018) 34–44.
[33] U. Stucki, J. Schmid, C.F. Hammerle, N.P. Lang, Clin. Oral. Implants Res. 12 (2001) 121–127.
[34] H.C. Blair, Q.C. Larrouture, Y. Li, H. Lin, D. Beer-Stoltz, L. Liu, R.S. Tuan, L. J. Robinson, P.H. Schlesinger, D.J. Nelson, Tissue Eng. Part B Rev. 23 (2017) 268–280.
[35] Y. Wang, W. Zhang, Q. Yao, J. Orthop. Transl. 29 (2021) 60–71.
[36] A.P. Kusumbe, S.K. Ramasamy, R.H. Adams, Nature 507 (2014) 323–328.
[37] L. Luo, S. Wang, Y. Hu, L. Wang, X. Jiang, J. Zhang, X. Liu, X. Guo, Z. Luo, C. Zhu, M. Xie, Y. Li, J. You, F. Yang, ACS Nano 17 (2023) 22508–22526.
[38] J. Pei, L. Cai, F. Wang, C. Xu, S. Pei, H. Guo, X. Sun, J. Chun, X. Cong, W. Zhu, Z. Zheng, X. Chen, Circ. Res. 131 (2022) 388–403.
[39] A.B. Jaykumar, S. Plumber, D.M. Barry, D. Binns, C. Wichaidit, M. Grzemska, S. Earnest, E.J. Goldsmith, O. Cleaver, M.H. Cobb, Proc. Natl. Acad. Sci. USA 119 (2022) e2203743119.
[40] Y.Y. Niu, Y.Y. Zhang, Z. Zhu, X.Q. Zhang, X. Liu, S.Y. Zhu, Y. Song, X. Jin, B. Lindholm, C. Yu, Cell Death Dis. 11 (2020) 211.
[41] K. Liu, L. Yang, X. Wang, Q. Huang, K. Tuerhong, M. Yang, R. Zhang, Y. Li, S. Yang, J. Clin. Periodontol 50 (2023) 368–379.
[42] Y.Y. Li, H.R. Peng, W.Y. Tang, D. Gu, S.S. Ren, Y.J. Yu, J. Yang, L.Y. Miao, Mater. Des. 225 (2023) 111540.
[43] M. Wojtas, A.J. Lausch, E.D. Sone, Proc. Natl. Acad. Sci. USA 117 (2020) 12636–12642.
[44] M. Zhang, X. Zhai, T. Ma, Y. Huang, M. Jin, H. Yang, H. Fu, S. Zhang, T. Sun, X. Jin, Y. Du, C.H. Yan, ACS Nano 17 (2023) 4433–4444.
[45] H. Heydari, S.E. Moosavifard, S. Elyasi, M. Shahraki, Appl. Surf. Sci. 394 (2017) 425–430.